

Velocity-map imaging for emittance characterization of multiphoton-emitted electrons from a gold surface

Hong Ye,^{1,2} Sebastian Trippel,^{1,3,*} Michele Di Fraia,^{1,3,†} Arya Fallahi,¹
Oliver D. Mücke,^{1,3} Franz X. Kärtner,^{1,2,3} and Jochen Küpper^{1,2,3}

¹Center for Free-Electron Laser Science, Deutsches Elektronen-Synchrotron DESY, Notkestraße 85, 22607 Hamburg, Germany

²Department of Physics, University of Hamburg, Luruper Chaussee 149, 22761 Hamburg, Germany

³The Hamburg Center for Ultrafast Imaging, University of Hamburg, Luruper Chaussee 149, 22761 Hamburg, Germany

(Dated: March 7, 2024)

A velocity-map-imaging spectrometer is demonstrated to characterize the normalized transverse emittance of photoemitted electron bunches. The two-dimensional (2D) projected velocity distribution images of photoemitted electrons are recorded by the detection system and analyzed to obtain the normalized transverse emittance. With the presented distribution function of the electron photoemission angles a mathematical method is implemented to reconstruct the three-dimensional (3D) velocity distribution curve. As a first example, multiphoton emission from a planar Au surface is studied via irradiation at a glancing angle by intense 45 fs laser pulses at a central wavelength of 800 nm. The reconstructed energy distribution agrees very well with the Berglund-Spicer theory of photoemission. The normalized transverse emittance of the intrinsic electron bunch is characterized to be 0.52 and 0.05 $\pi \cdot \text{mm} \cdot \text{mrad}$ in X - and Y -directions, respectively.

PACS numbers: 79.60.Bm, 41.20.Cv, 85.60.Ha, 79.20.Ws

I. INTRODUCTION

Time-resolved imaging of both transient molecular structure and condensed phase dynamics with picometer-femtosecond spatiotemporal resolution has recently become possible with the advent of x-ray free-electron lasers (XFELs) [1–7]. The high x-ray brilliance, coherence, and ultrashort pulse durations available from these sources are the key properties [8] that open up unprecedented opportunities for new science. Therefore, precise control of the x-ray pulse characteristics, including spectral coverage and temporal and spatial beam profiles are of utmost importance for advanced applications. These parameters are directly influenced by the properties of the electron bunch generating the x-ray pulses. Therefore, the accurate characterization of the electron beam quality is indispensable for assessing available approaches in order to enable improvements of the underlying electron beam technology. In addition, high quality electron bunches are instrumental in experiments where materials are studied using electron diffractive imaging [9–12].

The key measure in electron beam quality is electron beam emittance, i.e., the transverse phase-space distribution of the generated electron bunches. To quantify electron beam emittance as a function of photocathode composition and emission mechanisms, we demonstrate a velocity-map-imaging (VMI) spectrometer that allows us to directly access the transverse momentum distribution of photoemitted electrons, enabling the measurement of normalized transverse emittance from various

cathodes. Usually, emission mechanisms are classified as thermionic emission, photoemission, or tunneling emission under extraordinarily high electric fields. More recently, nanostructured and plasmonic photocathodes used with multiphoton or strong-field optical emission have been used as improved electron sources [13–18]. Both, the experimental characterization and the theoretical description of the electron emittance from such cathodes is highly important, which motivates the direct VMI measurements developed here.

As a first proof-of-principle example, we report on quantitative measurements of multiphoton emission from a 400 nm thick Au thin film at room temperature, which was excited with 45-fs laser pulses centered at 800 nm. These measurements additionally allowed us to benchmark the performance of this new experimental setup. Quantum-yield-dependent measurements were performed by recording the events of electrons impinging on the detector when varying the average laser power and the polarization angle, respectively. These experimental results confirm that four-photon emission occurs from the planar Au surface. In our experiments the 2D transverse velocity/momentum distribution of photoemitted electrons was directly imaged onto the detector. An experimental 3D energy distribution was reconstructed from the measured 2D VMI data using a mathematical algorithm (*vide infra*) and compared to the theoretically derived 3D-space energy distribution from the Berglund-Spicer photoemission model [19–22]. The very good agreement of our experimental results with the theoretical model demonstrates the applicability of VMI for the characterization of the normalized transverse emittance of photoelectron emitters.

* Email: sebastian.trippel@cfel.de

† Present address: Elettra-Sincrotrone Trieste S.C.p.A., 34149, Basovizza, Trieste, Italy

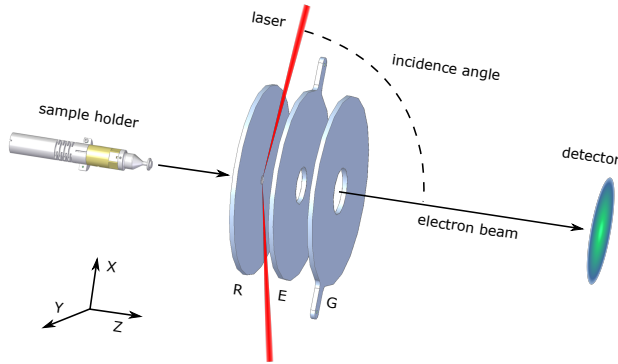


FIG. 1. Schematic of the velocity-map-imaging (VMI) spectrometer consisting of three parallel electrodes, R: repeller, E: extractor, G: ground. The sample is mounted on the top of the holder, which can be retracted from this main chamber into a load-lock chamber.

II. EXPERIMENTAL SETUP

The velocity-mapping technique maps the velocity coordinates of particles onto a 2D detector without, to first order, the influence of the spatial coordinates. To achieve this, a configuration of electrostatic lenses, in the simplest case using three parallel electrodes, is employed to spatially tailor the electric fields [23–25]. The electric fields can be also used to image and magnify the spatial coordinates suppressing the effect of velocity coordinates, which is then referred to as spatial-map imaging (SMI) [23]. The spectrometer demonstrated here aims to characterize the electron emittance via characterizing the average spread of electron coordinates in position-and-momentum phase space.

The schematic of the spectrometer is shown in Fig. 1. The sample is mounted on the top of the sample holder, which can be retracted into a load-lock chamber. The load lock is designed for exchanging the sample without breaking the ultra-high vacuum (UHV) of the imaging system. When performing the electrostatic imaging experiments, the sample holder is transferred into the main chamber and brought in contact with the repeller plate to make sure they are at the same electric potential. The main chamber, maintained at 10^{-9} mbar, contains a stack of three cylindrically symmetric plates, labelled repeller (R), extractor (E) and ground (G) electrodes in Fig. 1. They are arranged in parallel, separated by 15 mm, and, with applied potentials, serve as the electrostatic lens. This is followed by a ~ 0.5 m drift tube, which ends with a detector assembly consisting of a double micro-channel plate (MCP, Chevron configuration), a phosphor screen (P46), and a CMOS camera (Optronis CL600 $\times 2$) for recording images of the electron distributions. The full configuration is shielded against stray fields by a μ -metal tube. A 800-nm 45-fs Ti:Sapphire laser amplifier with a 3-kHz repetition rate was used to illuminate the sample at a glancing incidence angle of $\sim 84^\circ$, with a laser focal inten-

sity spot size of $\sim 17 \times 160 \mu\text{m}^2$ root-mean-square (RMS) on the sample. In our experiments, single-shot electron-distribution images are read out at a repetition rate of 1 kHz, limited by the camera-acquisition frame rate. The average number of electrons emitted per pulse is on the order of one or less, thus, space charge effects, which were reported before [26], are excluded.

To calibrate and optimize the spectrometer field configuration for both SMI and VMI, a fixed potential of -6 kV was applied to both the repeller plate and the sample holder while the ground plate being grounded; see supplementary information for details. While scanning the extractor voltage from -5.8 kV to -4.3 kV, we observed the focusing behavior of the electron bunch depending on the extractor voltage [27]. This behavior is revealed by the RMS of the electron bunch size in X - and Y -directions on the detector shown in Fig. S1 (supplementary information). The SIMION [28] software is used to simulate the electric field configuration and to calculate the electron trajectories from a 2D Gaussian source with $\sigma_X = 140 \mu\text{m}$ and $\sigma_Y = 15 \mu\text{m}$, yielding an RMS behavior curve that fits the experimental results. SMI is obtained at the minimum RMS size, i.e., at an extractor voltage of -5560 V, corresponding to a magnification factor of 7.5. From the measured SMI data, the RMS size is analyzed to be $\sigma_X = 158 \mu\text{m}$ and $\sigma_Y = 20 \mu\text{m}$, which is in good agreement with the simulated electron bunch size and the laser focal spot size. The extractor voltage for VMI conditions is found at -4790 V according to the SIMION simulations and the calibration factor of velocity-per-pixel is 8014 m/s/pixel on the detector. The details of the simulations and experimental calibration are described in the supplementary material. In order to minimize field distortions, the sample front surface should be placed in the same plane as the repeller front surface. However, samples of different thickness lead to a position offset with reference to the repeller front, which strongly influences the field configuration. Therefore, the extractor voltage for operating in SMI and VMI mode are optimized by voltage adjustments of [50, -50] V and [400, -200] V, respectively, to correct for a position offset of [-0.5, 0.5] mm. In this case, re-adjusting the potential right after exchanging a sample is necessary, but quick (*vide infra*).

III. EXPERIMENTAL RESULTS

Fig. 2a shows the photoemitted electron yield as a function of incident laser energy on a logarithmic scale. The data, shown in red, were measured and averaged over four measurement sequences and the error bars show the corresponding standard deviations of the photoemitted electron counts due to laser fluctuations. The blue line reflects the results of a linear regression analysis that yielded a slope of $c_x \approx 3.94$, with a standard error of 0.04 and a coefficient of determination $R^2 \approx 0.999$.

The Fowler-Dubridge model for the n -th order pho-

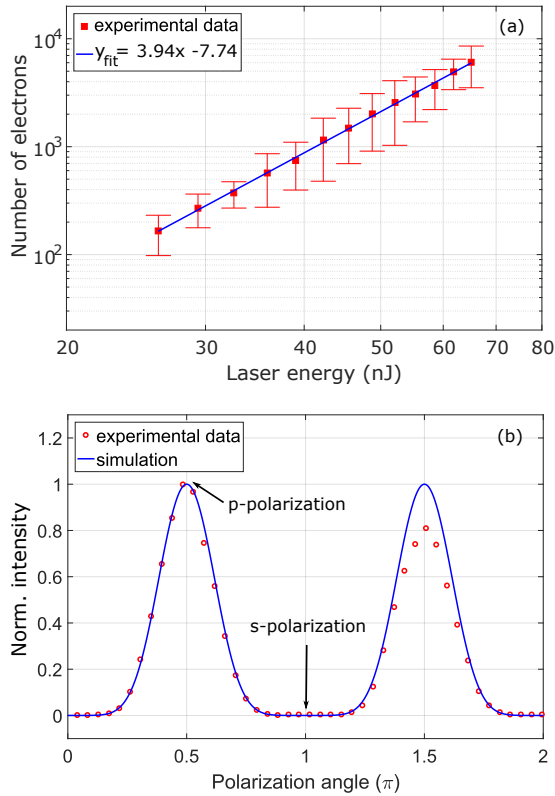


FIG. 2. Counts of the photoemitted electrons as function of (a) laser average power and (b) laser polarization angle. The experimental data for polarization angles $> \pi$ is of reduced quality due to laser drifting, etc., within the errorbar plot in (a).

toelectric current can be written in a generalized form as [29]

$$J \propto A(1 - R)^n I^n F\left(\frac{nh\nu - e\phi}{kT}\right) \quad (1)$$

where n is the number of photons, h is the Planck constant, A is the Richardson coefficient, R the reflection coefficient from the metal surface, I the incident light intensity, ϕ the metal work function, and $F(x) = \int_0^\infty \ln(1 + e^{-(y+x)}) dy$ the Fowler function.

The experimental data in Fig. 2a follow a power law with a slope of ~ 4 , in agreement with a 4-photon emission process according to the nonlinear photoelectric effect, which indicates that simultaneous absorption of 4 photons (photon energy 1.55 eV at 800 nm) has to take place to overcome the metal work function W [30], which is reported as 5.31–5.47 eV for Au [31]. As shown in Fig. 2b, varying the laser polarization angle, the photoemitted electron intensity reaches a maximum when the laser is p-polarized (electric field normal to the sample surface), and appears minimum when it is s-polarized. For multiphoton emission at a certain incident light intensity,

the electron yield mostly depends on the bulk absorption coefficient, expressed as term $(1 - R)^n$ in the Fowler-Dubridge model [30]. R is calculated by Fresnel equations with $n_1 = 1$ and $n_2 = 0.189 + i4.71$ [32] at an incidence angle of 84° . The plotted $(1 - R)^4$ curve fits very well with the data, which proves again the 4-th order multiphoton process.

A velocity-map image from a planar Au surface is shown in the inset of Fig. 3a. The image was integrated over 6×10^4 laser shots with an energy of ~ 50 nJ, corresponding to a peak intensity of 4×10^{10} W/cm² on the cathode. Generally, in laser-induced multiphoton emission the emitted electron velocity vectors exhibit cylindrical symmetry along the direction normal to the sample surface. Therefore, the center of mass (COM) of the image is set as coordinate origin. The corresponding angle-integrated radial velocity distribution of the projected electrons is plotted in Fig. 3a as black line. To allow for comparison with the theoretical model, the 3D velocity/energy distribution is required. Introducing a novel mathematical method similar to the Onion Peeling algorithm [33], we are able to reconstruct the momentum/energy distribution when the angular distribution of emitted electrons is known. Fortunately, for multiphoton emission, the intensity of photoemitted electrons at various angles θ can be derived from the Berglund-Spicer model [20] as

$$I(\theta) \propto \aleph^2 \cos \theta \cdot \frac{1}{1 + \alpha l(E)} \cdot \frac{1}{\sqrt{1 - \aleph^2 \cdot \sin^2 \theta}} \quad (2)$$

where α is the optical absorption coefficient, $l(E)$ is the electron-electron scattering length for an electron of kinetic energy E , and \aleph expresses the electron analogy of refraction at the vacuum-metal boundary [34]. For a small \aleph (our case, $\aleph = 0.275$), i. e., an incident photon energy $nh\nu$ comparable to the work function W , the equation can be simplified to $I(\theta) \propto \cos \theta$ [35, 36]. Therefore, the 3D velocity distribution can be reconstructed as is described in detail in the supplementary information.

The reconstructed velocity distribution is plotted as blue line in Fig. 3a, and the smoothed energy distribution shown in Fig. 3b. The energy distribution of the emitted electrons shows an energy spread of ~ 1 eV, which corresponds to the energy difference between a four-1.55 eV-photon excitation and the Au work function of 5.31 eV.

IV. DISCUSSION

The Berglund-Spicer three-step model is employed as the analytic expression for the kinetic energy distribution of the photoemitted electrons. As the model is derived for single-photon emission, it is implied in our analysis that the electrons at an initial energy state E_0 absorb sufficient number of photons instantaneously, rather than sequentially, to be pumped to a higher energy state $E = E_0 + nh\nu$. The kinetic energy distribution for single-photon emission [19] is adapted to multiphoton emission

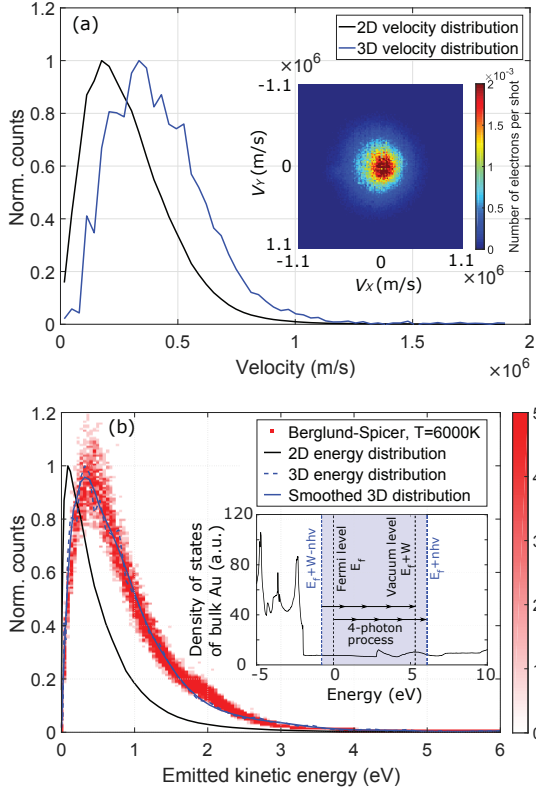


FIG. 3. (a) Projected 2D (black curve) and reconstructed 3D (blue curve) radial velocity distribution of the measured velocity-map image that is shown in the inset. (b) Reconstructed kinetic-energy distribution and its simulation using the Berglund-Spicer model assuming an electron temperature of 6000 K. The colorbar represents the probabilities of photoelectron kinetic energies due to the photon-energy spectrum of the laser. The inset shows the density of states calculated for bulk Au, which is used in the Berglund-Spicer model simulation. The blue area depicts the four-photon-ionization range.

as

$$N(E) dE \propto \frac{K C(E) \alpha}{\alpha + 1/l(E)} dE \times \left[1 + 4 \left(\frac{E - E_f}{nh\nu} - 1 + \ln \frac{nh\nu}{E - E_f} \right) \right] \quad (3)$$

where E_f is the Fermi energy of Au. $C(E) = 0.5 \times (1 - \sqrt{W/E})$ for $E \geq W$ is a semiclassical threshold function. $l(E)$ is the electron-electron scattering length, which is proportional to $E^{-3/2}$. The absorption coefficient α is calculated from the extinction coefficient $k = 4.71$ as $\alpha = 4\pi k/\lambda$ and taken as a constant $\alpha = 7.7 \times 10^5 \text{ cm}^{-1}$ independent of electron energy. K is a correction factor related to both $C(E)$ and $\alpha l(E)$, which is between 0.5 to 1. To evaluate Equation 3, the probability of a photon

carrying energy $h\nu$ is calculated from the measured laser spectrum in the range from 760 to 850 nm. To overcome the barrier of 5.31 eV, an electron is assumed to always absorb four photons ($n \equiv 4$). Absorption of various photon energies leads to slight difference of the quantum yield at a certain emitted kinetic energy as one can see from Fig. 3 b. The main consequence of absorbing photons with various energies is the spectral/intensity broadening, which is illustrated by the color coding in Fig. 3 b, but with an essentially unchanged spectral shape. We mention that (3) only includes the emitted electrons that experience none or one electron-electron scattering process during transport to the metal-vacuum surface. Electron-electron scattering is dominant over electron-phonon scattering and reshapes the energy distribution on a fast timescale, i.e., during an ultrashort laser pulse.

The density of states (DOS), i.e., the number of states available for electrons at a certain energy level, is shown in the inset of Fig. 3 b. During the photoemission process, an energy state E_0 is first occupied by an electron, which is then excited to a higher energy state E , which was empty. As fermions, electrons obey the Pauli exclusion principle. In thermal equilibrium, the possibility of electrons to occupy an available energy state is given by the Fermi-Dirac (FD) distribution f_{FD} . However, excitation of a metal with ultrashort strong laser pulses initially creates a nonequilibrium distribution that then thermalizes via electron-electron scattering towards a Fermi-Dirac distribution. In gold, this thermalization occurs on a timescale of hundreds of femtoseconds [37, 38]. Subsequently, the electrons cool down by dissipating energy into the lattice via electron-phonon scattering occurring on a longer picosecond timescale. In the following discussion, where we employ the Berglund-Spicer model in our analysis, we assume that the electronic system can be described by a Fermi-Dirac distribution with quasi-equilibrium electron temperature T_e . Hence, the appropriate densities of states and FD distributions are multiplied with the energy distribution as $N(E) dE f_{\text{FD}}(E_0) \text{DOS}(E_0) (1 - f_{\text{FD}}(E)) \text{DOS}(E)$, resulting in the spectrum shown in Fig. 3 b.

The best fit with our reconstructed experimental energy distribution is obtained for an electron temperature of 6000 K. This is comparable to previously observed electron temperatures of 7000 K in surface-enhanced multiphoton emission from copper [39]. The high energy tail of the spectrum indicates that very “hot” electrons are photoemitted by the femtosecond laser pulse, consistent with the high excess energy deposited into the electronic system. For the energy tail up to 4 eV, except for the high temperature, another process that might need to be taken into account is above-threshold photoemission (ATP), i.e., the absorption of one (or more) extra photon, occurring together with the four-photon process [40]. Moreover, for our experimental conditions, we can neglect tunnel ionization, which could result in high energy emitted electrons. Since we estimate the absorbed peak intensity for the recorded image, Fig. 3 a, to be $\sim 4 \times 10^9 \text{ W/cm}^2$

taking into account Fresnel losses. This implies a Keldysh parameter $\gamma = \sqrt{W/2U_p} \approx 17 \gg 1$, which is well in the multiphoton emission regime; here, $U_p \propto \lambda^2 I$ is the ponderomotive energy with laser wavelength λ and intensity I .

Since both, the measured quantum yield and the momentum distribution, are in quantitative agreement with the Fowler-Dubridge and Berglund-Spicer models, as one would expect from multiphoton emission from a planar Au cathode, the VMI spectrometer has successfully been implemented as a tool to characterize the photoemitted electrons from cathodes, especially to directly measure the transverse momentum distribution. Assuming there is no correlation between the location of emission and the transverse momentum, the RMS normalized emittance ϵ_n is defined as [34]

$$\epsilon_{n_\zeta} = \frac{\sqrt{\langle \zeta^2 \rangle \langle p_\zeta^2 \rangle}}{mc}, \text{ with } \zeta \in \{X, Y\} \quad (4)$$

where $\langle \zeta^2 \rangle$ is the spatial spread and $\langle p_\zeta^2 \rangle$ is the momentum spread of the electron bunch. From the velocity map image shown in the inset of Fig. 3a, the RMS normalized emittance of the planar Au photocathode irradiated by 45-fs 800-nm laser pulses with a focal spot size of $\sigma_X = 161 \mu\text{m}$ and $\sigma_Y = 17 \mu\text{m}$ is characterized to be $\epsilon_{n_X} = 0.52 \pi \cdot \text{mm} \cdot \text{mrad}$ and $\epsilon_{n_Y} = 0.05 \pi \cdot \text{mm} \cdot \text{mrad}$ in the X and Y -directions, respectively. To decrease the intrinsic normalized emittance, in principle one needs to decrease either the emission area or the momentum spread. The former can be intuitively decreased by an extremely tight focal spot size or sharp tip surface, which geometrically limits the emission area. For reducing of the momentum/energy spread, choosing a proper material with appropriate work function and irradiated by a laser beam with matched photon energy, for example the photoemission of Cu under 266-nm laser irradiation, is expected to help. Further reduction is expected when entering the strong-field emission regime, where the electrons are considered to adiabatically tunnel through the surface barrier with zero initial momentum and are then driven by the instantaneous optical field [13, 41]. Under these conditions electrons are expected to be emitted with a relatively small divergence angle and significantly lower transverse momentum spread.

V. CONCLUSIONS

We demonstrated an electron spectrometer with VMI and SMI capabilities, which intuitively allows for the

measurement of the normalized transverse emittance of photocathodes. i.e., through the direct observation of the transverse position and momentum distributions. We verified and benchmarked the capabilities of the instrument in a proof-of-concept experiment, in which we characterized the photoemitted electrons from a 400 nm thin Au film. For ultrashort femtosecond laser pulses with a peak intensity lower than 10^{12} W/cm^2 at 800 nm central wavelength, which would correspond to $\gamma = 1$, multiphoton emission is shown to be the dominant contribution to the entire electron current.

We intend to utilize this new setup for the emittance characterization of electron bunches strong-field emitted from nanotips under optical field irradiation. Such devices should show superior emittance [14, 17]. Moreover, the small radius of the sharp tips realize a field enhancement, which dramatically lowers the laser power required for entering the strong-field regime and thus avoids damaging of the cathodes. Our ongoing work aims at the characterization of electron emission from nanostructured array emitters, which are predicted to provide high-current low-emittance coherent electron bunches in the strong-field emission regime.

VI. ACKNOWLEDGMENTS

We gratefully acknowledge helpful discussions with Jens S. Kienitz and Nele Müller, the expert technical support of Thomas Tilp, and Nicolas Tancogne-Dejean for providing the computed density-of-states data of bulk Au.

Besides DESY, this work has been supported by the excellence cluster “The Hamburg Center for Ultrafast Imaging – Structure, Dynamics and Control of Matter at the Atomic Scale” (CUI, DFG-EXC1074), the priority program QUTIF (SPP1840 SOLSTICE) of the Deutsche Forschungsgemeinschaft, the European Research Council under the European Union’s Seventh Framework Programme (FP7/2007-2013) through the Consolidator Grant COMOTION (ERC-Küpper-614507) and the Synergy Grant AXISIS (ERC-Kaertner-609920), the Helmholtz Association “Initiative and Networking Fund”, and the accelerator on a chip program (ACHIP) funded by the Betty and Gordon Moore foundation.

[1] H. N. Chapman, A. Barty, M. J. Bogan, S. Boutet, S. Frank, S. P. Hau-Riege, S. Marchesini, B. W. Woods, S. Bajt, W. H. Benner, London W. A., E. Plönjes, M. Kuhlmann, R. Treusch, S. Düsterer, T. Tschentscher,

J. R. Schneider, E. Spiller, T. Möller, C. Bostedt, M. Hoener, D. A. Shapiro, K. O. Hodgson, D. van der Spoel, F. Burmeister, M. Bergh, C. Caleman, G. Hultdt, M. M. Seibert, F. R. N. C. Maia, R. W. Lee, A. Szöke,

- N. Timneanu, and J. Hajdu, “Femtosecond diffractive imaging with a soft-x-ray free-electron laser,” *Nat. Phys.* **2**, 839–843 (2006).
- [2] Anton Barty, Sebastien Boutet, Michael J. Bogan, Stefan Hau-Riege, Stefano Marchesini, Klaus Sokolowski-Tinten, Nikola Stojanovic, Ra’anan Tobey, Henri Ehrke, Andrea Cavalleri, Stefan Düsterer, Matthias Frank, Săsa Bajt, Bruce W. Woods, M. Marvin Seibert, Janos Hajdu, Rolf Treusch, and Henry N. Chapman, “Ultrafast single-shot diffraction imaging of nanoscale dynamics,” *Nat. Photon.* **2**, 415 (2008).
- [3] L Young, E P Kanter, Bertold Kraessig, Y Li, A M March, S T Pratt, R Santra, S. H. Southworth, N Rohringer, L F DiMauro, Gilles Doumy, C A Roedig, N Berrah, L Fang, M Hoener, P H Bucksbaum, J P Cryan, S Ghimire, J M Glownia, D A Reis, J D Bozek, C Bostedt, and M Messerschmidt, “Femtosecond electronic response of atoms to ultra-intense x-rays,” *Nature* **466**, 56 (2010).
- [4] Anton Barty, Carl Caleman, Andrew Aquila, Nicusor Timneanu, Lukas Lomb, Thomas A White, Jakob Andreasson, David Arnlund, Săsa Bajt, Thomas R M Barends, Miriam Barthelmess, Michael J Bogan, Christoph Bostedt, John D Bozek, Ryan Coffee, Nicola Coppola, Jan Davidsson, Daniel P Deponte, R Bruce Doak, Tomas Ekeberg, Veit Elser, Sascha W Epp, Benjamin Erk, Holger Fleckenstein, Lutz Foucar, Petra Fromme, Heinz Graafsma, Lars Gumprecht, Janos Hajdu, Christina Y Hampton, Robert Hartmann, Andreas Hartmann, Günter Hauser, Helmut Hirsemann, Peter Holl, Mark S Hunter, Linda Johansson, Stephan Kassemeyer, Nils Kimmel, Richard A Kirian, Mengning Liang, Filipe R N C Maia, Erik Malmerberg, Stefano Marchesini, Andrew V Martin, Karol Nass, Richard Neutze, Christian Reich, Daniel Rolles, Benedikt Rudek, Artem Rudenko, Howard Scott, Ilme Schlichting, Joachim Schulz, M Marvin Seibert, Robert L Shoeman, Raymond G Sierra, Heike Soltau, John C H Spence, Francesco Stellato, Stephan Stern, Lothar Strüder, Joachim Hermann Ullrich, X Wang, Georg Weidenspointner, Uwe Weierstall, Cornelia B Wunderer, and Henry N Chapman, “Self-terminating diffraction gates femtosecond x-ray nanocrystallography measurements,” *Nat. Photon.* **6**, 35–40 (2012).
- [5] Benedikt Rudek, Sang-Kil Son, Lutz Foucar, Sascha W. Epp, Benjamin Erk, Robert Hartmann, Marcus Adolph, Robert Andritschke, Andrew Aquila, Nora Berrah, Christoph Bostedt, Nicola Bozek, Johnand Coppola, Frank Filsinger, Hubert Gorke, Tais Gorkhover, Heinz Graafsma, Lars Gumprecht, Andreas Hartmann, Günter Hauser, Sven Herrmann, Helmut Hirsemann, Peter Holl, Andre Hömke, Loic Journal, Christian Kaiser, Nils Kimmel, Faton Krasniqi, Kai-Uwe Kühnel, Michael Matyssek, Marc Messerschmidt, Danilo Miesner, Thomas Möller, Robert Moshhammer, Kiyonobu Nagaya, Bjorn Nilsson, Guillaume Potdevin, Daniel Pietschner, Christian Reich, Daniela Rupp, Gerhard Schaller, Ilme Schlichting, Carlo Schmidt, Florian Schopper, Sebastian Schorb, Claus-Dieter Schröter, Joachim Schulz, Marc Simon, Heike Soltau, Lothar Strüder, Kiyoshi Ueda, Georg Weidenspointner, Robin Santra, Joachim Ullrich, Artem Rudenko, and Daniel Rolles, “Ultra-efficient ionization of heavy atoms by intense x-ray free-electron laser pulses,” *Nat. Photon.* **6**, 858–865 (2012).
- [6] Anton Barty, Jochen Küpper, and Henry N. Chapman, “Molecular imaging using x-ray free-electron lasers,” *Annu. Rev. Phys. Chem.* **64**, 415–435 (2013).
- [7] Benjamin Erk, Rebecca Boll, Sebastian Trippel, Denis Anielski, Lutz Foucar, Benedikt Rudek, Sascha W Epp, Ryan Coffee, Sebastian Carron, Sebastian Schorb, Ken R Ferguson, Michele Swiggers, John D Bozek, Marc Simon, Tatiana Marchenko, Jochen Küpper, Ilme Schlichting, Joachim Ullrich, Christoph Bostedt, Daniel Rolles, and Artem Rudenko, “Imaging charge transfer in iodomethane upon x-ray photoabsorption,” *Science* **345**, 288–291 (2014).
- [8] Zhirong Huang and Kwang Je Kim, “Review of x-ray free-electron laser theory,” *Phys. Rev. ST Accel. Beams* **10**, 1–26 (2007).
- [9] H Ihée, VA Lobastov, UM Gomez, BM Goodson, R Srinivasan, CY Ruan, and Ahmed H Zewail, “Direct imaging of transient molecular structures with ultrafast diffraction,” *Science* **291**, 458–462 (2001).
- [10] B J Siwick, J R Dwyer, R E Jordan, and R J Dwayne Miller, “An atomic-level view of melting using femtosecond electron diffraction,” *Science* **302**, 1382–1385 (2003).
- [11] Max Gulde, Simon Schweda, Gero Storeck, Manisankar Maiti, Hak Ki Yu, Alec M Wodtke, Sascha Schäfer, and Claus Ropers, “Ultrafast low-energy electron diffraction in transmission resolves polymer/graphene superstructure dynamics,” *Science* **345**, 200–204 (2014).
- [12] Jie Yang, Markus Guehr, Xiaozhe Shen, Renkai Li, Theodore Vecchione, Ryan Coffee, Jeff Corbett, Alan Fry, Nick Hartmann, Carsten Hast, Kareem Hegazy, Keith Jobe, Igor Makasyuk, Joseph Robinson, Matthew S Robinson, Sharon Vetter, Stephen Weathersby, Charles Yoneda, Xijie Wang, and Martin Centurion, “Diffractive imaging of coherent nuclear motion in isolated molecules,” *Phys. Rev. Lett.* **117**, 153002 (2016).
- [13] Michael Krüger, Markus Schenk, and Peter Hommelhoff, “Attosecond control of electrons emitted from a nanoscale metal tip,” *Nature* **475**, 78–81 (2011).
- [14] G Herink, D R Solli, M Gulde, and C Ropers, “Field-driven photoemission from nanostructures quenches the quiver motion,” *Nature* **483**, 190–193 (2012).
- [15] Anna Mustonen, Paul Beaud, Eugenie Kirk, Thomas Feuerer, and Soichiro Tsujino, “Five picocoulomb electron bunch generation by ultrafast laser-induced field emission from metallic nano-tip arrays,” *Astrophys. Lett. & Comm.* **99**, 103504 (2011).
- [16] William P Putnam, Richard G Hobbs, Phillip D Keathley, Karl K Berggren, and Franz X Kärtner, “Optical-field-controlled photoemission from plasmonic nanoparticles,” *Nat. Phys.* **13**, 335–339 (2016).
- [17] Soichiro Tsujino, Prat Das Kanungo, Mahta Monshipouri, Chiwon Lee, and R.J. Dwayne Miller, “Measurement of transverse emittance and coherence of double-gate field emitter array cathodes,” *Nat. Commun.* **7**, 13976 (2016).
- [18] F. X. Kärtner, F. Ahr, A. L. Calendron, H. Çankaya, S. Carbajo, G. Chang, G. Cirmi, K. Dörner, U. Dorda, A. Fallahi, A. Hartin, M. Hemmer, R. Hobbs, Y. Hua, W. R. Huang, R. Letrun, N. Matlis, V. Mazalova, O. D. Mücke, E. Nanni, W. Putnam, K. Ravi, F. Reichert, I. Sarrou, X. Wu, A. Yahaghi, H. Ye, L. Zapata, D. Zhang, C. Zhou, R. J D Miller, K. K. Berggren, H. Graafsma, A. Meents, R. W. Assmann, H. N. Chapman, and P. Fromme, “Axisis: Exploring the frontiers in attosecond x-ray science, imaging and spectroscopy,” *Nucl. Instrum. Meth. A* **829**, 24–29 (2016).
- [19] C. N. Berglund and W. E. Spicer, “Photoemission studies

- of copper and silver: Theory,” *Phys. Rev.* **136**, A1030 (1964).
- [20] C. N. Berglund and W. E. Spicer, “Photoemission studies of copper and silver: Experiment,” *Phys. Rev.* **136**, A1044–A1064 (1964).
- [21] W. F. Krolkowski and W. E. Spicer, “Photoemission studies of the noble metals. i. copper,” *Phys. Rev. B* **185**, 882–900 (1969).
- [22] W. F. Krolkowski and W. E. Spicer, “Photoemission studies of the noble metals. ii. gold,” *Phys. Rev. B* **1**, 478–487 (1970).
- [23] André T. J. B. Eppink and David H. Parker, “Velocity map imaging of ions and electrons using electrostatic lenses: Application in photoelectron and photofragment ion imaging of molecular oxygen,” *Rev. Sci. Instrum.* **68**, 3477–3484 (1997).
- [24] A I Chichinin, K H Gericke, S Kauczok, and C Maul, “Imaging chemical reactions — 3d velocity mapping,” *Int. Rev. Phys. Chem.* **28**, 607–680 (2009).
- [25] M. Stei, J. von Vangerow, R. Otto, A. H. Kelkar, E. Carascosa, T. Best, and R. Wester, “High resolution spatial map imaging of a gaseous target,” *J. Chem. Phys.* **138**, 214201 (2013).
- [26] Guillaume Petite, Pierre Agostini, Rusty Trainham, Eric Mevel, and Philippe Martin, “Electron emission from metals under laser irradiation,” *Phys. Rev. B* **45**, 12 210 – 12 217 (1992).
- [27] Nele L. M. Müller, Sebastian Trippel, Karol Długołęcki, and Jochen Küpper, “Electron gun for diffraction experiments on controlled molecules,” *J. Phys. B* **48**, 244001 (2015), arXiv:1507.02530 [physics].
- [28] Scientific Instrument Services Inc., USA, “Simion 8.1,” (2011), URL: <http://simion.com>.
- [29] J. H. Bechtel, W. L. Smith, and N. Bloembergen, “Four-photon photoemission from tungsten,” *Opt. Comm.* **13**, 56–59 (1975).
- [30] A Damascelli, G Gabetta, A Lumachi, L Fini, and F Parmigiani, “Multiphoton electron emission from Cu and W: An angle-resolved study,” *Phys. Rev. B* **54**, 6031–6034 (1996).
- [31] David R. Lide, *CRC Handbook of Chemistry and Physics*, 84th ed. (CRC Press, 2003).
- [32] Mikhail N. Polyanskiy, “Refractive index database,” <https://refractiveindex.info>, accessed on 24. July 2017.
- [33] Cameron J. Dasch, “One-dimensional tomography: a comparison of Abel, onion-peeling, and filtered backprojection methods,” *Applied Optics* **31**, 1146 (1992).
- [34] David H. Dowell and John F. Schmerge, “Quantum efficiency and thermal emittance of metal photocathodes,” *Phys. Rev. ST Accel. Beams* **12**, 074201 (2009).
- [35] R. T. Poole, R. C. G. Leckey, J. G. Jenkin, and J. Liesegang, “Photoelectron angular distribution from gold,” *J. Elec. Spec. Rel. Phen.* **2**, 371–376 (1972-1973).
- [36] Zeting Pei and C. Neil Berglund, “Angular distribution of photoemission from gold thin films,” *Jpn. J. Appl. Phys.* **41**, L52–L54 (2002).
- [37] W. S. Fann, R. Storz, H. W K Tom, and J. Bokor, “Direct measurement of nonequilibrium electron-energy distributions in sub-picosecond laser-heated gold films,” *Phys. Rev. Lett.* **68**, 2834–2837 (1992).
- [38] W. S. Fann, R. Storz, H. W K Tom, and J. Bokor, “Electron thermalization in gold,” *Phys. Rev. B* **46**, 13592–13595 (1992), arXiv:1011.1669 [physics].
- [39] M. Aeschlimann, C. A. Schmuttenmaer, H. E. Elsayed-Ali, R. J. D. Miller, J. Cao, Y. Gao, and D. A. Mantell, “Observation of surface enhanced multiphoton photoemission from metal surfaces in the short pulse limit,” *J. Chem. Phys.* **102**, 8606–8613 (1995).
- [40] Francesco Banfi, Claudio Giannetti, Gabriele Ferrini, Gianluca Galimberti, Stefania Pagliara, Daniele Fausti, and Fulvio Parmigiani, “Experimental evidence of above-threshold photoemission in solids,” *Phys. Rev. Lett.* **94**, 037601 (2005), arXiv:1201.3049 [physics].
- [41] P. B. Corkum, “Plasma perspective on strong-field multiphoton ionization,” *Phys. Rev. Lett.* **71**, 1994–1997 (1993).

Supplementary information: Velocity-map imaging for emittance characterization of multiphoton-emitted electrons from a gold surface

Hong Ye,^{1,2} Sebastian Trippel,^{1,3,*} Michele Di Fraia,^{1,3,†} Arya Fallahi,¹
Oliver D. Mücke,^{1,3} Franz X. Kärtner,^{1,2,3} and Jochen Küpper^{1,2,3}

¹Center for Free-Electron Laser Science, Deutsches Elektronen-Synchrotron DESY, Notkestraße 85, 22607 Hamburg, Germany

²Department of Physics, University of Hamburg, Luruper Chaussee 149, 22761 Hamburg, Germany

³The Hamburg Center for Ultrafast Imaging, University of Hamburg, Luruper Chaussee 149, 22761 Hamburg, Germany

(Dated: March 7, 2024)

I. SPECTROMETER CHARACTERIZATION

The electron spectrometer has been characterized experimentally, accompanied by simulations, in order to determine the focusing conditions for the SMI and VMI modes; see Fig. 1 in the main manuscript for the experimental setup. Fig. S1 shows the measured root-mean-square (RMS) in the X - and Y -directions of the spatial electron distribution on the detector as a function of the extractor voltage, together with the results from SIMION [1] electric field and particle trajectory simulations. A similar behavior as in Ref. 2 is observed.

The strongest focusing of the electron bunch onto the detector is achieved at an extractor potential of -5560 V, which is thus identified as the SMI voltage. The RMS at this voltage shows the magnified laser-surface-interaction area. The slightly different focusing behavior of the electron bunch in the X and Y -directions is attributed to the asymmetric initial electron bunch size, due to the glancing

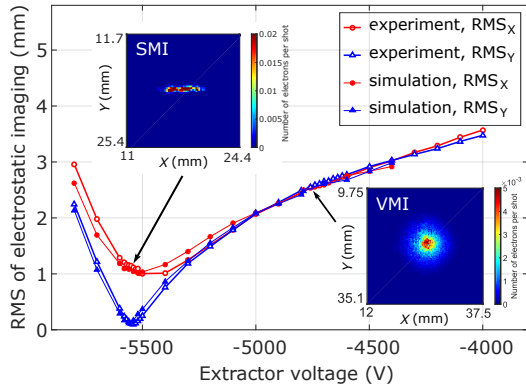


FIG. S1. Experimental (hollow) and simulated (solid) root-mean-square deviations of electron spatial distributions on the 2D detector versus focusing extractor voltage in both X and Y -directions. The insets show SMI and VMI detector images for the indicated positions.

* Email: sebastian.trippel@cfel.de

† Present address: Elettra-Sincrotrone Trieste S.C.p.A., 34149, Basovizza, Trieste, Italy

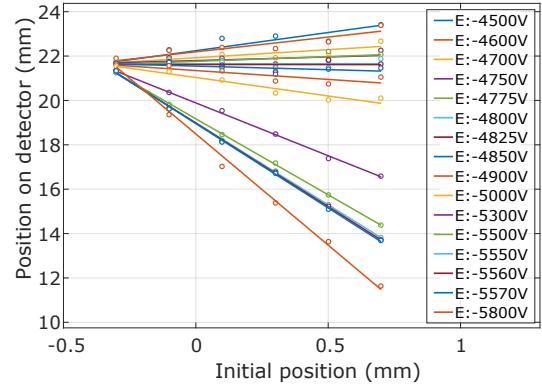


FIG. S2. Position dependence of the center of mass of the electrostatic imaging on the detector on the initial source position for various extractor potentials from -5800 V to -4500 V.

incidence irradiation, and the finite kinetic energy of the electrons.

When increasing the extractor voltage, the electron bunch diverges. Based on our simulations, the extractor voltage for VMI is approximately -4790 V. For a full calibration of the spectrometer, the simulations were used to study the field configuration and the electron trajectories in those fields for the given electrode configurations and the particles initial distributions. In Fig. S1 the simulated RMS of the electron bunch, with electrostatic imaging, at the detector position is plotted as function of extractor voltage. The simulations were carried out given an initial spatial 2D Gaussian distribution of 2000 electrons for each simulated point. The center of mass (COM) of this distribution was given by $(X, Y) = (0, 0)$ and a Z -coordinate matching the sample surface with standard deviations of $\sigma_X = 140 \mu\text{m}$ and $\sigma_Y = 15 \mu\text{m}$. The initial momentum distribution was given by a uniform half sphere with an uniform kinetic energy distribution of electrons in the range of $[0.1, 0.6]$ eV.

The COM of the electron distribution as a function of the initial starting position of the electrons, i. e., the laser focus position on the sample, was used to experimentally calibrate the voltage for velocity-map imaging. Fig. S2 shows the COM as function of the laser position for various voltages together with straight-line fits. A decrease of

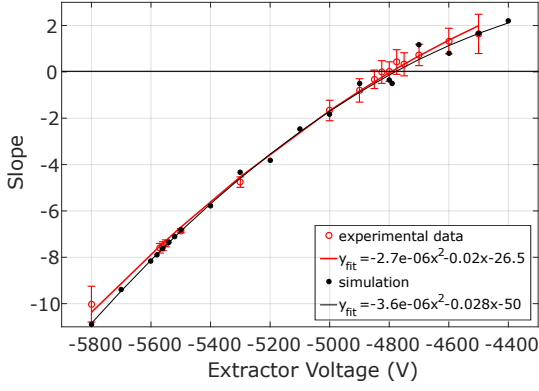


FIG. S3. Slope of the experimental laser position dependent COM of the spatial distribution at the detector as function of the extractor voltage (red circles) with a quadratic fit (red line). Black points and the black line indicate the corresponding simulated results.

the slope with decreasing extractor voltage is observed. Fig. S3 depicts the slope of each measurement in Fig. S2 as function of the extractor voltage together with a quadratic fit and corresponding simulation results. The error bar for the experimental points is given by the first-order coefficient error of each fitting curve with 95 % confidence bounds. VMI mode is obtained at the zero crossing of this curve, i.e., at -4790 V, as for this voltage the distribution, to first order, becomes independent of the starting position. The data shows a good agreement with the simulations, confirming that the extractor voltage for operating the VMI is -4790 V. From the simulations the imaging setup is calibrated regarding the transverse electron velocities to 8014 m/s/pixel on the detector. The resulting voltages for operation in the SMI and VMI modes are listed in Table I.

Fig. S4 shows experimental and theoretical COM of the electron distribution at the detector as function of the lens position, that is used to focus the laser beam onto the sample for SMI (E:-5560 V). The straight lines are fits to the data. The difference in the slope between the X- and Y-directions is due to the glancing incidence angle θ . The laser spot position on sample moves $1/\cos\theta$ times farther in X than in Y when displacing the laser beam the same distance by a translation stage. For the Y-direction we obtain a magnification factor of ~ 7.5 from the fit. For the X-direction a slope of ~ 72.7 is obtained. This results in a ratio of 9.7 between the two slopes that corresponds to

TABLE I. Voltages (in V) applied for operation in SMI and VMI mode

	Repeller	Extractor	Ground	Sample
SMI	-6000	-5560	0	-6000
VMI	-6000	-4790	0	-6000

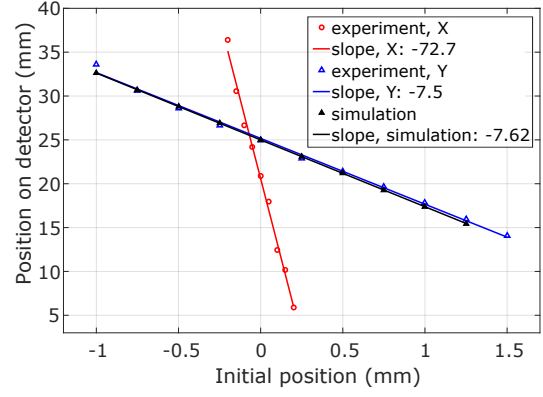


FIG. S4. The COM of electrostatic imaging on the detector as a function of the initial source position for SMI mode, i.e., an extractor voltage of -5560 V. The slope in Y-direction is the spatial magnification factor. The ratio between X- and Y-directions confirms the incidence angle of the laser beam of 84° .

an incident angle of 84° . The SIMION simulation results, also shown in Fig. S4, are in good agreement with the data.

The focusing conditions for the SMI and VMI mode depend strongly on the position of the sample inside the velocity-map imaging spectrometer. Fig. S5 shows the simulated extractor voltages necessary for SMI and VMI mode for various sample displacements with respect to the front surface of the repeller plate. These simulations show that either the sample position has to be known, or at least be reproduced, to a very high precision or calibration measurements have to be performed when a new sample is inserted into the spectrometer. Fortunately, with the protocol described in our manuscript this calibration can be done quickly. In addition the dependence

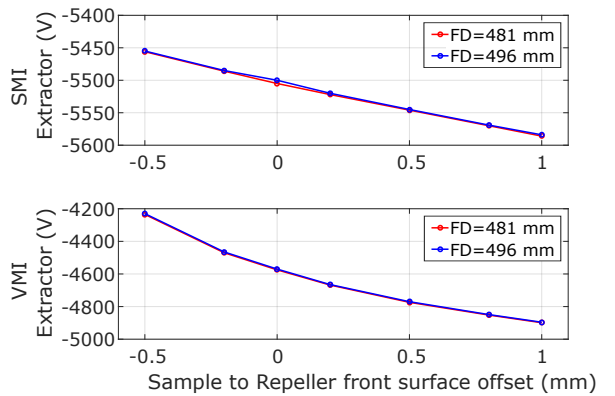


FIG. S5. Top: SMI and bottom: VMI extractor potential for different position offset from sample front to the repeller front surfaces. FD stands for flying distance in the figure legend.

of the extractor voltage on the flight distance has been investigated (red points and lines). Our simulations show that this uncertainty is uncritical compared to the exact sample position in the spectrometer.

II. RECONSTRUCTION ALGORITHM

Our reconstruction algorithm for the conversion of the 2D projected velocity distribution to the 3D distribution is based on the assumption that the angular distribution of the photoemitted electrons is known. For our simulations, a cosine function $I(\theta) \propto \cos \theta$ [3, 4], derived from the Berglund-Spicer model [5] as discussed in the main text, is applied in the algorithm. In addition, it is assumed that for multiphoton emission the angular distribution is independent of the modulus of the three dimensional velocity vector. The 3D velocity distribution is then obtained from the 2D projected distribution by a matrix method similar to Onion Peeling [6]. For multiphoton emission from a planar Au surface, the electrons are assumed to be photoemitted within a half sphere of $\varphi \in [0, 2\pi]$, $\theta \in [0, \pi/2]$. The photoemitted electron distribution has cylindrical symmetry with respect to the surface normal of the sample.

Fig. S6 a shows a scatter plot for a single 3D velocity v_i distribution given by $f(v, \theta) = \delta(v - v_i) \cos \theta$. Fig. S6 b shows the projection of this distribution onto the 2D detector surface. It can be derived that the projected velocity distribution for this special case is

$$P_i(v_x, v_y) = \int f(v, \theta) dv_z = \begin{cases} C & \text{for } v_{x,y} < v_i, \\ 0 & \text{otherwise} \end{cases}$$

where C is a constant. As shown in Fig. S6 b, the projected velocity distribution of $f(v, \theta)$ is constant inside the circular phase-space area of radius v_i . Furthermore, Fig. S6 c shows the radial distribution obtained from the projected velocity distribution given by

$$\rho_i(v_{2D}) = \int P_i(v_x, v_y) d\theta_{2D} = \begin{cases} 2\pi C \cdot v_{2D} & \text{for } v_{2D} < v_i \\ 0 & \text{otherwise} \end{cases}$$

where $v_{2D} = \sqrt{v_x^2 + v_y^2}$. In the reconstruction, each radial distribution $\rho_i(v_{2D})$ is built up by a triangle as sketched in Fig. S6 d. v_i is taken equally spaced and form the intervals confined by the neighboring gray dashed lines. The 2D projected distribution is related to the 3D

distribution f_i by a transfer matrix \mathbf{M} .

$$\rho_i = \mathbf{M} f_i, \quad (1)$$

with \mathbf{M} given by:

$$\mathbf{M} = \begin{pmatrix} 1 & 1/4 & 1/9 & 1/16 & \dots \\ 0 & 3/4 & 3/9 & 3/16 & \dots \\ 0 & 0 & 5/9 & 5/16 & \dots \\ 0 & 0 & 0 & 7/16 & \dots \\ \vdots & \vdots & \vdots & \vdots & \ddots \end{pmatrix} \quad (2)$$

The 3D distribution can finally be obtained by inversion of the measured 2D-projected distribution

$$f_i = \mathbf{M}^{-1} \rho_i. \quad (3)$$

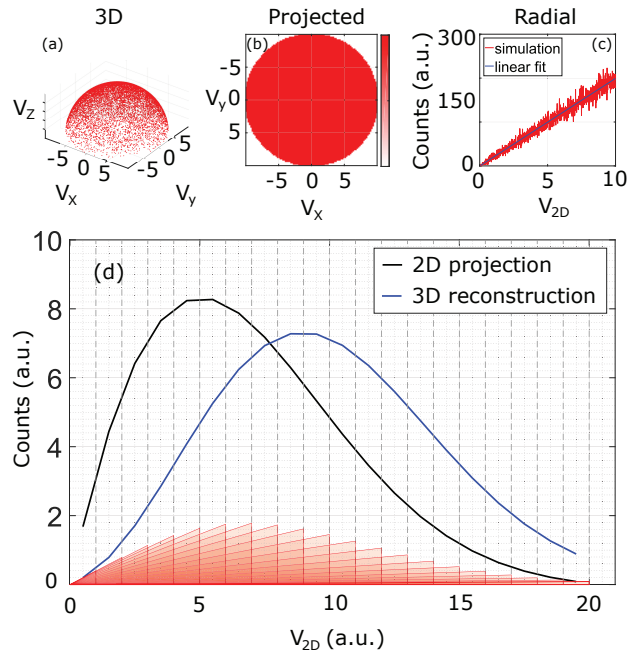


FIG. S6. (a-c) Representation of a simulated electron bunch with a single 3D velocity v_i and an angular distribution of a cosine function: (a) in 3D, forming a spherical surface; (b) in 2D, yielding a uniform distribution in the detector plane; (c) in 1D, showing a linearly increasing radial velocity v_{2D} with distance from distribution COM. (d) A conceptual diagram of the reconstruction algorithm: The area of each red triangle at the bottom indicates the number of photoemitted electrons having the same 3D velocity. The corresponding distribution curve is plotted as blue curve. The black curve is the 2D projection distribution curve, summing up the number of photoemitted electrons within each interval of the same transverse velocity. The gray dashed lines indicate the transverse-velocity intervals used in this projection.

- [2] Nele L. M. Müller, Sebastian Trippel, Karol Długołęcki, and Jochen Küpper, “Electron gun for diffraction experiments on controlled molecules,” *J. Phys. B* **48**, 244001 (2015), arXiv:1507.02530 [physics].
- [3] R. T. Poole, R. C. G. Leckey, J. G. Jenkin, and J. Liesegang, “Photoelectron angular distribution from gold,” *J. Elec. Spec. Rel. Phen.* **2**, 371–376 (1972-1973).
- [4] Zeting Pei and C. Neil Berglund, “Angular distribution of photoemission from gold thin films,” *Jpn. J. Appl. Phys.* **41**, L52–L54 (2002).
- [5] C. N. Berglund and W. E. Spicer, “Photoemission studies of copper and silver: Experiment,” *Phys. Rev.* **136**, A1044–A1064 (1964).
- [6] Cameron J. Dasch, “One-dimensional tomography: a comparison of Abel, onion-peeling, and filtered backprojection methods,” *Applied Optics* **31**, 1146 (1992).